JOURNAL OF GEOPHYSICAL RESEARCH, VOL. 106, NO. D21, PAGES 27,497–27,507, NOVEMBER 16, 2001

Surface and tethered-balloon observations of actinic flux: Effects of arctic stratus, surface albedo, and solar zenith angle

Stephan R. de Roode, Peter G. Duynkerke, Wim Boot, and Jeroen C. H. Van der Hage

Institute for Marine and Atmospheric Research Utrecht, Utrecht University, Utrecht, Netherlands

Abstract. As part of the First ISCCP Regional Experiment (FIRE III) Arctic Cloud Experiment actinic flux measurements were made above the Arctic Sea ice during May 1998. The actinic flux, which is also referred to as the 4π radiative flux, is the relevant radiative parameter needed to determine photodissociation rates. It is shown that for a plane-parallel cloud the change in the net irradiance as a function of the optical depth is proportional to the magnitude of the actinic flux. Continuous actinic flux measurements were made just above the snow-covered ice surface by a UV-A and a visible 4π radiometer (wavelengths ~365 and ~550 nm, respectively). In addition, vertical profiles of the actinic flux through low arctic stratus clouds were obtained by means of a visible 4π radiometer suspended under a tethered balloon. The cloud thermodynamic and microphysical structure was determined from observations made by the National Center for Atmospheric Research C-130 aircraft. In addition, the phase and liquid water path of the cloud was assessed from microwave radiometer, lidar, and radar data. During clear-sky conditions the diurnal variation of the magnitude of actinic flux was controlled mainly by Rayleigh scattering and surface reflection. Above a stratus cloud layer the actinic flux was found to be almost the same as during clear-sky conditions. This could be attributed to the fact that the effective albedo of the arctic sea ice and the cloud is only slightly higher than the ground albedo alone. In the arctic stratus clouds the actinic flux was found to be nearly constant with height, except in a shallow layer near the cloud top where the actinic flux increased significantly with height. The vertical profiles that were observed in arctic stratus differed from those measured in Atlantic stratocumulus; in the latter the actinic flux was found to increase gradually from cloud base to cloud top. A delta-Eddington model is utilized to illustrate that the exact shape of the vertical profile is very sensitive to the solar zenith angle. During the arctic experiments the solar zenith angle was generally much larger than during the observations in Atlantic stratocumulus.

1. Introduction

To study the change in the concentration of a chemical reactive species in the atmosphere, one needs to solve an elaborate set of equations describing chemical reactions. Many of these chemical reactions are driven by solar radiation as a result of photodissociation [*Crutzen and Zimmermann*, 1991]. The radiative parameter that determines the photodissociation rate of chemical species is the actinic flux, which is defined as the incident radiance integrated over all solid angles [*Madronich*, 1987]. The actinic flux therefore concerns the probability of an encounter between a photon and a molecule, whereas the irradiance describes the flow of radiant energy through the atmosphere [*Zeng et al*., 1996]. Thus radiance incident from all directions contributes to the actinic flux and for this reason the actinic flux is also referred to as the mean intensity, or the 4π radiative flux.

The actinic flux is not a simple linear function of the irradiance. It depends on how much of the downwelling radiation is direct or diffuse and on the amount of upward reflected radiation [*Madronich*, 1987; *Ruggaber et al*., 1993; *Van Weele and Duynkerke*, 1993; *Zeng et al*., 1996; *Los et al*., 1997; *Landgraf and Crutzen*, 1998]. Actinic fluxes have been observed by *Junkermann* [1994], *Shetter et al*. [1996], *McKenzie et al*. [1998], and *Van Weele et al*. [1995]. These studies showed that the actinic flux tends to increase when downwelling solar radiation is reflected by the ground surface or a cloud layer. *Vilà-Guerau de Arellano et al*. [1994] used a tethered balloon to collect measurements in an Atlantic stratocumulus cloud layer; their study showed that the actinic flux increased approximately linearly from cloud base to cloud top.

Actinic fluxes were measured by the Institute for Marine and Atmospheric Research Utrecht (IMAU) above the arctic sea ice at the Surface Heat Balance of the Arctic Ocean (SHEBA) ice camp (76°N, 166°W) during May 1998. This measurement campaign was part of the (First ISCCP (International Satellite Cloud Climatology Project) Regional Experiment) (FIRE III) Arctic Cloud Experiment, which was designed to address questions concerning clouds and radiation in the arctic sea ice region [*Curry et al*., 2000]. During the period of observation the arctic region was characterized by a high surface albedo, large solar zenith angles, and the frequent occurrence of low stratus clouds. UV-A and visible actinic fluxes, at wavelengths (λ) of 365 and 550 nm, respectively, were measured continuously by two 4π radiometers positioned just above the surface. Vertical profiles of the visible actinic flux were obtained at least once a day from a 4π radiometer attached to a tethered-balloon. Be-

Paper number 2001JD900236.
0148-0227/01/2001JD900236$09.00

cause the 4π radiometer aboard the balloon was identical to the one placed above the ice surface [*Van der Hage and de Roode*, 1999], it was possible to measure directly the difference between the visible actinic flux above and below the arctic stratus cloud. Cloud properties could be determined from in-situ observations collected by the National Center for Atmospheric Research (NCAR) C-130 aircraft. A microwave radiometer installed at the surface retrieved the cloud liquid water path. In addition, a radar and lidar were operational.

In section 2 some simple relations between the actinic flux and the irradiance will be derived for a plane-parallel cloud. We show that it might be possible to use in-cloud actinic flux observations to determine vertical absorption profiles of the net irradiance. In sections 3 and 4 the experimental setup is described, and the thermodynamic and microphysical structure of arctic stratus as observed from the NCAR C-130 research aircraft is discussed in detail. The measured diurnal cycle of the actinic flux is presented in section 5. To explore whether these findings are consistent with radiative transfer theory we compare them with results obtained with the Tropospheric Ultraviolet-Visible (TUV) radiation model [*Madronich*, 1993]. Input parameters required by the model such as cloud optical depth and ground surface albedo were all readily available from various measurement platforms at the SHEBA ice camp. In addition, vertical profiles of the actinic flux measured in arctic stratus clouds are shown in section 5. These are compared with the measurements made in Atlantic stratocumulus by *Vilà-Guerau de Arellano et al*. [1994]. The effects of the solar zenith angle and of the ground surface albedo on the shape of the in-cloud vertical profile are explained by use of a simple delta-Eddington model. A summary is given in section 6.

2. Theory

The total actinic flux (F_{tot}) can be computed by integrating the total radiance (I_{tot}) over all angles

$$F_{\mathrm{tot}} = \int_0^{2\pi} \int_{-1}^{1} I_{\mathrm{tot}}(\mu, \varphi)\, d\mu\, d\varphi, \tag{1}$$

where φ is the azimuth angle and μ is the cosine of the zenith angle θ measured from the positive (outward) surface normal. The total net irradiance E_{tot} is defined as

$$E_{\mathrm{tot}} = \int_0^{2\pi} \int_{-1}^{1} I_{\mathrm{tot}}(\mu, \varphi)\mu\, d\mu\, d\varphi. \tag{2}$$

In these definitions, I_{tot} represents the total radiance field due to the contribution of the direct solar beam I_0 and the diffuse radiance I_*. The diffuse upward (positive) and downward (negative) components of the actinic flux and irradiance are given by

$$\begin{aligned} F_{\pm} &= \int_0^{2\pi} \int_0^{1} I_*(\pm\mu, \varphi)\, d\mu\, d\varphi, \\ E_{\pm} &= \int_0^{2\pi} \int_0^{1} I_*(\pm\mu, \varphi)\mu\, d\mu\, d\varphi. \end{aligned} \tag{3}$$

Following these definitions, the total actinic flux and total irradiance can be rewritten as

$$\begin{aligned} F_{\mathrm{tot}} &= F_0 + F_- + F_+ = F_0 + F_*, \\ E_{\mathrm{tot}} &= -(E_0 + E_-) + E_+ = -E_0 + E_*, \end{aligned} \tag{4}$$

in which the subscript zero denotes the contribution from the direct solar beam, F_* is the total diffuse part of the actinic flux, and E_* indicates the net upward component of the diffuse irradiance. The solar zenith angle is denoted by θ_0, and we define $\theta_0 = \arccos(-\mu_0)$ such that $\mu_0 > 0$. The direct downward component of the solar irradiance (E_0) as a function of the optical depth (τ) is given by

$$E_0(\tau) = \mu_0 S_0\, e^{-\tau/\mu_0}, \tag{5}$$

where S_0 is the solar irradiance perpendicular to the direction of incidence at the top of the atmosphere, $\tau(z) = \int_z^{\infty} k(z')\, dz'$ the optical depth, z is the height above the ground surface, and k is the extinction coefficient. The direct components of the actinic flux and irradiance are related according to [*Madronich*, 1987]

$$F_0 = E_0/\mu_0. \tag{6}$$

An equation that expresses a simple relation between the irradiance and the actinic flux can be derived from the radiative transfer equation for the diffuse radiance $I(\tau, \mu, \varphi)$ which reads [*Goody and Yung*, 1989]

$$\begin{aligned} \mu \frac{dI(\tau, \mu, \varphi)}{d\tau} &= I(\tau, \mu, \varphi) - \frac{\omega_0}{4\pi} \int P(\mu, \varphi; \mu', \varphi') I(\tau, \mu', \varphi')\, d\omega' \\ &\quad - \frac{\omega_0}{4\pi} P(\mu, \varphi; -\mu_0, \varphi_0) S_0\, e^{-\tau/\mu_0} \end{aligned} \tag{7}$$

with z the height above the ground surface, ω_0 is the single scattering albedo, $d\omega = \sin\theta d\theta d\varphi$, and $P(\mu, \varphi; \mu', \varphi')$ is the phase function defining the light incident at (μ', φ'), which is scattered in the direction (μ, φ). By integrating (7) over $d\omega$ and by using (6), we obtain

$$\frac{dE_*}{d\tau} = (1 - \omega_0) F_* - \omega_0 \frac{E_0}{\mu_0}, \tag{8}$$

where we used a phase function P normalized to unity, $\int (P/4\pi)\, d\omega = 1$. Using (4), (5), and (6), we can rewrite (8)

$$\frac{dE_{\mathrm{tot}}}{d\tau} = (1 - \omega_0) F_{\mathrm{tot}}. \tag{9}$$

According to (9), if there is no absorption ($\omega_0 = 1$), then the total net irradiance will remain constant irrespective of changes in the optical depth, which means that radiative energy is conserved. However, for $0 < \omega_0 < 1$, and since F_{tot} is positive definite, the total net irradiance will become less negative toward cloud base, indicating that radiation is absorbed within the cloud layer. If the single scattering albedo is known very accurately, the change in the total net irradiance with height can then be found by measuring the total actinic flux and by integrating (9). A possible advantage of this approach is that the total net irradiance can be measured by only one 4π radiometer, rather than by two separate radiometers. Moreover, because radiance is not weighted by a factor $\cos\theta$ in the actinic flux, the orientation of 4π radiometers is not important,

whereas radiometers measuring irradiance need to be positioned perfectly horizontally.

Analogously, we can derive an equation which relates the total actinic flux to the gradient of the total net irradiance. If we multiply (7) by $\mu d\omega$, after integration we obtain

$$\int \mu^2 \frac{dI(\tau, \mu, \varphi)}{d\tau} d\omega = \int \mu I(\tau, \mu, \varphi)\, d\omega - \frac{\omega_0}{4\pi} \int\int \mu P(\mu, \varphi; \mu', \varphi') I(\tau, \mu', \varphi')\, d\omega'\, d\omega - \frac{\omega_0}{4\pi} \int \mu P(\mu, \varphi; -\mu_0, \varphi_0) S_0 e^{-\tau/\mu_0} d\omega. \quad (10)$$

To simplify (10), we will use the following approximation [*Goody and Yung*, 1989]:

$$\int \mu^2 \frac{dI(\tau, \mu, \varphi)}{d\tau} d\omega \approx \frac{1}{3} \frac{dF_*}{d\tau}, \quad (11)$$

and the relation

$$\frac{1}{4\pi} \int \mu P(\mu, \varphi; \mu', \varphi')\, d\omega' = g\mu', \quad (12)$$

with g the asymmetry factor [*Goody and Yung*, 1989]. Note that (11) is exact for the Eddington approximation. By substituting (11) and (12) into (10), we obtain

$$\frac{1}{3} \frac{dF_{\text{tot}}}{d\tau} = (1 - \omega_0 g) E_{\text{tot}} - E_0 \left(\frac{1}{3\mu_0^2} - 1 \right), \quad (13)$$

where we used (3)–(6). Equation (13) demonstrates the nonlinear dependency of the actinic flux gradient on the irradiance. If there is no absorption and the radiation is totally diffuse ($E_0 = 0$), the actinic flux decreases linearly from cloud top toward cloud base as a function of the optical depth, since $E_{\text{tot}} < 0$. If $\mu_0^2 \leq 1/3$ and $E_0 \geq 0$, F_{tot} will always decrease from cloud top toward cloud base. However, if $\mu_0^2 > 1/3$, the sign of the actinic flux gradient will depend on the relative magnitude of E_0 and E_{tot}.

3. Experimental Setup: Instrumentation and Measurement Site

The actinic flux measurements were performed during May 1998 as part of the FIRE arctic field program [*Curry et al*., 2000]. Continuous measurements were collected just above the surface. In addition, a tethered balloon with a visible 4π radiometer aboard was launched at least once a day from the SHEBA ice camp. The tethered-balloon observations also included wind velocity and direction, temperature, pressure, and relative humidity. The measurement frequency was 0.1 Hz. The average maximum altitude typically reached by the balloon was ~1 km, which was often sufficient to measure well above the tops of low stratus clouds. In addition, continuous surface observations were made of the upward and downward components of the longwave, shortwave and UV-B irradiance, UV-A, and visible actinic fluxes. The cloud water content and droplet effective radius in ground fog were measured by means of a Gerber PVM-100A that was positioned ~2.2 m above the surface. In order to obtain vertical profiles in the atmospheric surface layer, wind velocity and direction, temperature, and humidity were measured at five different levels from a 10-m-high meteorological mast [*Duynkerke and de Roode*, 2001].

The visible 4π radiometer used for this study was newly developed for the FIRE III experiment. It has a maximum spectral response in the visible light part of the spectrum at 550 nm and is described by *Van der Hage and de Roode* [1999]. Basically, the instrument consists of a spherical diffuser connected to a single photodiode by a light conductor. The directional response to light is largely isotropic. Two identical visible 4π radiometers were used, one being attached to a mast at 1.5 m above the surface and the other one being attached to a tethered balloon. To prevent the instrument from being shadowed, it was suspended by a small cable ~10 m below the balloon. Also, a newly rebuilt version of the UV-A 4π radiometer, described by *Van der Hage et al*. [1994], was placed above the ice surface. Since the single scattering albedo is nearly 1 for these wavelengths, cloud radiative absorption is negligibly small.

All the 4π radiometers were calibrated against results obtained with the monochromatic radiative transfer model TUV for clear-sky conditions by comparing the measurements with the model results for $\mu_0 = 0.5$. Clear-sky conditions were determined on the basis of the microwave radiometer, radar and lidar data, and visual observations. Under these circumstances, Rayleigh scattering and surface reflection are the primary mechanisms determining the magnitude of the actinic flux. However, even under clear skies, there can be scattering particles like ice crystals and aerosols. Because scattering tends to make the light diffuse, $\mu_0 = 0.5$ was chosen because at this angle the magnitude of the actinic flux does not depend on whether the light is direct or diffuse [*Madronich*, 1987]. The input parameters that need to be specified in the model are the vertical atmospheric profile of temperature, the surface pressure, and the albedo of the snow-covered sea ice. The measured broadband shortwave surface albedo at the site was ~0.8, which is a representative value for a pristine snow surface. Simultaneous measurements of the narrowband UV-B irradiance, however, indicated that the surface albedo for this waveband was ~0.9. The difference between the narrowband and broadband albedo corresponds to the results of a model study performed by *Wiscombe and Warren* [1980] and observations presented by *Grenfell et al*. [1994] for pristine snow. The latter study showed that for a broadband albedo of ~0.83 the spectral albedo for wavelengths within the range $0.3 \leq \lambda \leq 0.7$ μm is at least 10% larger. We therefore assumed an albedo of 0.9 to be representative for the UV-A and visible light albedo. The actinic flux measurements are estimated to be accurate within 10%.

Because FIRE, SHEBA, and the Atmospheric Radiation Measurement (ARM) interacted closely, various data sets that were collected near the SHEBA site are available. The NCAR C-130 aircraft took measurements near and above the SHEBA ice camp. Tethered-balloon launches were scheduled just before and just after the aircraft flew over the camp. To study the cloud microphysical structure, we used Forward Scattering Spectrometer Probe (FSSP-100) and 260X data from the aircraft. These instruments measure cloud droplet concentrations in different bin sizes. A microwave radiometer (MWR) operated at 23.8 and 31.4 GHz [*Liljegren*, 1994]. The 23.8-GHz channel, which is close to the water vapor spectral line at 22.235 GHz, is more sensitive to water vapor than cloud liquid water (and vice versa for the 31.4-GHz channel). Measure-

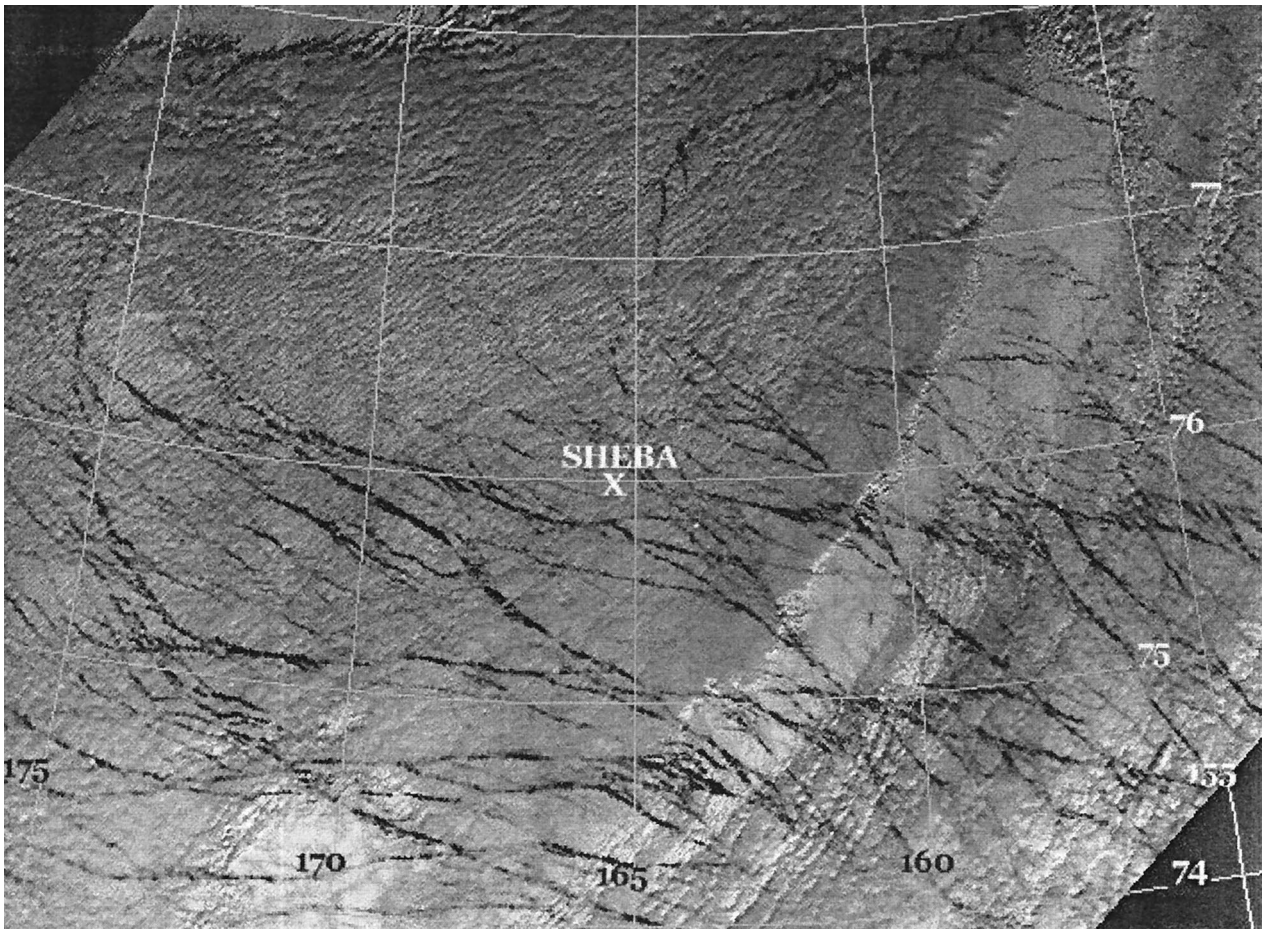

Figure 1a. NOAA AVHRR satellite images at 2219 UTC, May 7, 1998, over the SHEBA ice camp remapped to a polar stereographic project (1 km). The longitude ranges between 175°W and 155°W and the latitude ranges between 74°N and 78°N. Channel 1 (0.63 μm) visible satellite image. Black lines are old cracks in the ice that have refrozen. Whiter parts of the image are clearer areas than the darker (cloudier) parts. Ice patterns are poorly visible to the northwest of the ice station because of the denser arctic stratus cloud.

ments of the sky radiance at these two frequencies allow the simultaneous determination of the water vapor path and liquid water path (W) from a set of two linear equations. In principle, these two channels are not very sensitive to the presence of ice, but they are sensitive to deep cloud layers with a substantial amount of large ice crystals that scatter radiation in the 23.8- and 31.4-GHz frequencies [*Adler et al*., 1990]. The total cloud optical depth τ_c can be computed by [*Stephens*, 1984]

$$\tau_c = 3W/2\rho_l r_e, \tag{14}$$

where ρ_l is the density of liquid water and r_e is the cloud droplet effective radius. The latter could be determined from the aircraft data. During SHEBA the NOAA vertically pointing Depolarization and Backscatter Unattended Lidar (DABUL) operated almost continuously, providing information about the cloud phase (J. M. Intrieri et al., Annual cycle of arctic cloud statistics from lidar and radar at SHEBA, submitted to *Journal of Geophysical Research*, 2001).

4. Meteorological Conditions

Between May 7 and 9, 1998 (Julian Day 127–129), a persistent low-stratus deck, capped by a strong thermal inversion, was present at the SHEBA ice camp. According to the visible light image made by the NOAA satellite (Figures 1a and 1b), there are extended white areas intersected by black lines, which are refrozen cracks in the sea ice. These cracks open frequently and cause a strong surface flux of heat and moisture, since the temperature of the open water is just slightly below 0°C [*Pinto et al*., 1995]. Early in the month of May, two leads opened in the vicinity of the measurement site, several hundred meters wide. These leads froze and reopened intermittently during the month, but during the latter half of the month, virtually no open water could be seen in the vicinity of the experimental site. To the northwest of the ice station, the cracks are poorly visible because of the denser arctic stratus clouds. At first glance, however, it is hard to distinguish from Figure 1a whether the white area is covered by clouds or snow only because the visible reflectance of a snow-covered ice surface is virtually the same as that of a cloud overlying a snow-covered ice surface. On the right of the visible image (Figure 1a), there is a whiter spot; the same area looks black in the infrared image and is indicated in Figure 1b as a "clear" area. In the infrared image (Figure 1b) the whiter areas represent high clouds which make a much larger thermal contrast with the snow-covered sea ice than the low stratus clouds.

An example of the vertical potential temperature structure in arctic stratus is presented in Figure 2. The nearly constant

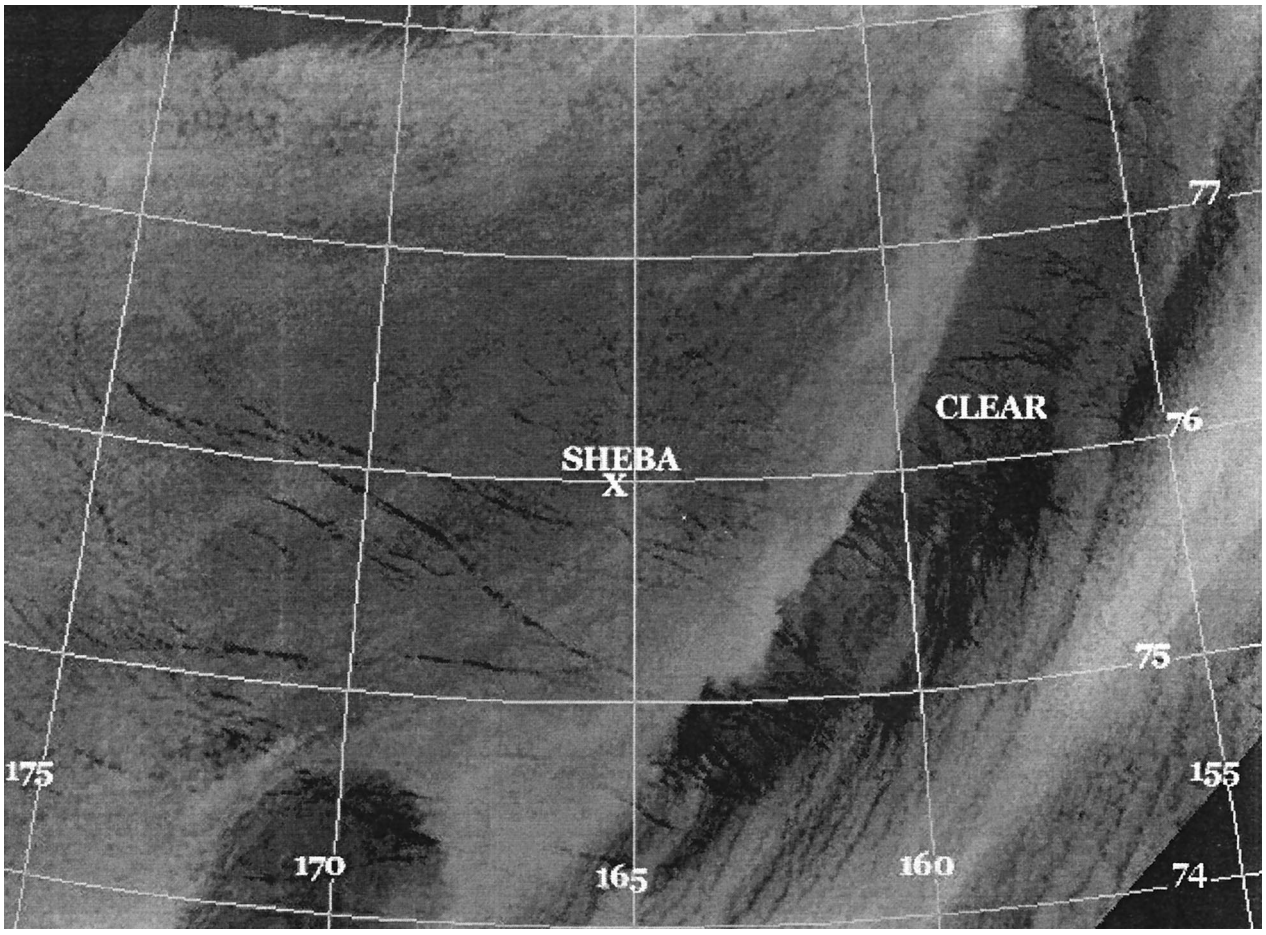

Figure 1b. Same as Figure 1a for infrared channel 4 (11 μm). Darker parts of the image are clearer areas than the lighter (cloudier) parts. Ice patterns cannot be seen through the optically denser (whiter) clouds.

potential temperature in the boundary layer is a feature which is remarkably different from a vertical profile made in subtropical stratus or stratocumulus clouds. Because the wet-adiabatic lapse rate approaches the dry-adiatic lapse rate when temperatures are well below freezing, it is hard to distinguish a pronounced wet-adiabatic vertical temperature profile in this arctic cloud layer. The time variations of the potential temperature in the boundary layer and free atmosphere were

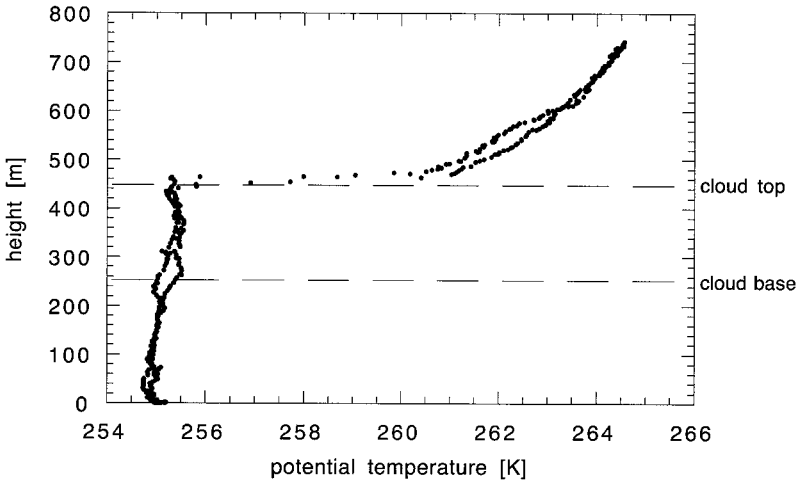

Figure 2. Vertical potential temperature profile measured from the tethered balloon on May 7, 1998, around 1800 UTC. The approximate cloud base (260 m) and cloud top (450 m) during the balloon sounding are indicated.

very small; on average, an upward and downward balloon sounding took ~1 hour, and during this period the difference in potential temperature at the same height was <0.5°C.

The NCAR C-130 aircraft flew above the SHEBA ice camp just after the balloon sounding. Cloud droplet size distributions were measured by an FSSP-100 (with a diameter (d) range $1.9 < d < 55.5$ μm) and by a 260X probe. From the latter we used data from intervals $60.4 < d < 846.4$ μm only; thus measurements from the smallest bins were neglected to prevent overlaps with the FSSP bins. Neither instrument can distinguish whether the collected particles are in the ice or liquid water phase. To compute the liquid and ice water content and the cloud droplet effective radius, it was assumed that the droplets were spherical. This assumption is not very accurate as far as large particles which are detected by the 260X are concerned. These are probably ice or snow particles, but as can be seen in Figure 3a, their contribution to the ice and liquid water content (IWC and LWC, respectively) is relatively low, as is their number concentration. The results of the IWC and LWC shown in Figure 3a are the averages of all data collected within height intervals of 10 m. In order to filter effects caused by instrumental noise we computed the cloud droplet effective radius and the droplet number concentration only when IWC + LWC > 0.001 g m^{-3}. If we define this threshold to distinguish between clear and cloudy air, we find that between 290 and 380 m the cloud fraction was about unity. The total IWC and LWC in the cloud layer is due primarily to the smaller droplets which were measured by the FSSP. As a result, r_e above cloud base (~300 m during the aircraft measurements) is relatively small and of the order of 5 μm. This relatively small number is due to a rather high cloud ice and liquid water droplet concentration of ~250 cm^{-3}.

Herman and Curry [1984] presented droplet spectra of arctic stratus clouds and concluded that the clouds had a wide range of microphysical properties; they reported values for the total cloud droplet concentration as large as 512 cm^{-3}. In the subcloud layer the larger particles measured by the 260X dominate, as is clear from the contribution they make to the IWC and LWC. As a consequence, r_e is ~1 order of magnitude larger than in the cloud layer. These results are similar to observations made in marine stratocumulus [*Duynkerke et al.*, 1995]. They concluded that within the cloud layer the liquid water content was due mainly to the smaller droplets, whereas in the subcloud layer larger droplets dominated, making a negligibly small contribution to the liquid water content but on the other hand causing a significant amount of drizzle.

Figure 4 shows the cloud optical depth computed by (14), where we used $r_e = 5$ μm according to the aircraft measurements and MWR data for the liquid water path. The cloud layer tended to become optically thinner around the time of maximum solar elevation around 2300 UTC. Usually arctic stratus clouds are predominantly optically thin [*Curry et al.*, 2000]. Because the cloud droplet effective radius was relatively low, rather high maximum values were found for the total cloud optical depth ($\tau_c \approx 20$). These maxima were typically observed during small μ_0. Since the MWR is insensitive to the presence of ice these results indicate that a significant fraction of the cloud particles consisted of liquid water droplets in spite of the relatively cold temperatures in the cloud (about −18°C). The lidar depolarization ratio δ can serve as an indicator of cloud phase. Nearly spherically symmetrical and optically homogeneous scatterers, such as cloud and drizzle drops, generate near-zero depolarization of the incident energy in the exact backscattering direction, whereas scatterers with the arbitrary geometry of ice particles generate values which are typically in the range $\delta \approx 0.4 \sim 0.5$ [*Sassen*, 1991]. The lidar depolarization ratio was small for this period ($\delta < 0.1$), suggesting that the cloud phase was predominantly liquid. Analyses of other NCAR C-130 data measured during SHEBA suggested that in the absence of ice particles falling from above, the occurrence of ice in boundary layer clouds appears to be related to maximum droplet sizes [*Curry et al.*, 2000]. These observations and measurements reported by *Hobbs and Rangno* [1998] suggest that the chance that clouds do not contain ice particles increases for larger droplet concentrations (typically >100 cm^{-3}).

5. Observations and Computations of Actinic Flux

5.1. Diurnal Cycle

In Figure 5 observed actinic fluxes for a clear-sky day ($\tau = 0$) are presented and compared with model results. The observed actinic fluxes are slightly smaller than the model results. By taking $\tau = 0$, we implicitly assumed that aerosols and ice crystals may be neglected as scattering particles. However, it is likely that the neglect of these particles can explain the slight overestimation of the modeled actinic flux. For example, if a very small optical depth was used in the model, namely, $\tau = 0.1$, a better agreement was found between the observed and modeled UV-A and visible actinic fluxes. In Figure 5 we also plotted the theoretical value of the actinic flux for the special case of zero optical depth and zero ground surface albedo. For that case, from (5) and (6), we would expect the actinic flux to be constant with time and independent of the solar zenith angle. The observations show that even for small μ_0 the actinic flux above the arctic sea ice is larger than the direct component of the actinic flux at the top of the atmosphere. The likely explanation is that the high surface albedo (α) acts to strongly increase the upward component of the radiation, which, by (1), enhances the total actinic flux. *Van Weele et al.* [1995] presented UV-A actinic flux measurements made during clear-sky conditions for both a snow-covered surface ($\alpha = 0.9$) and a grass surface ($\alpha = 0.05$). They concluded that the effect of the snow was to nearly double the actinic flux compared to the actinic flux results found above the grass surface.

Figure 6a depicts the observed actinic flux above stratus clouds and surface observations during both clear and cloudy skies. The surface observations during cloudy skies and one of the balloon soundings (case 5) were made simultaneously. The actinic flux above the cloud is nearly the same as during the clear-sky observations. This can be explained by the fact that the effective albedo of the arctic sea ice and the cloud is only slightly larger than the ground albedo alone. Below the cloud, however, the actinic flux is lower than during clear-sky conditions. To examine the effect of cloud optical thickness on the actinic flux, a series of simulations with the TUV radiation model were performed, varying the solar zenith angle and optical thickness (Figure 6b). We assumed a perfectly clear sky above the cloud ($\tau = 0$). The actinic flux above the cloud hardly depends on the optical thickness of the cloud. Below the cloud there is a clear tendency towards a lower actinic flux with increasing optical thickness. The observations and the model results show a qualitatively similar behavior. This should be the case since throughout the observational period the optical thickness varied between 5 and 20. The model predicts a

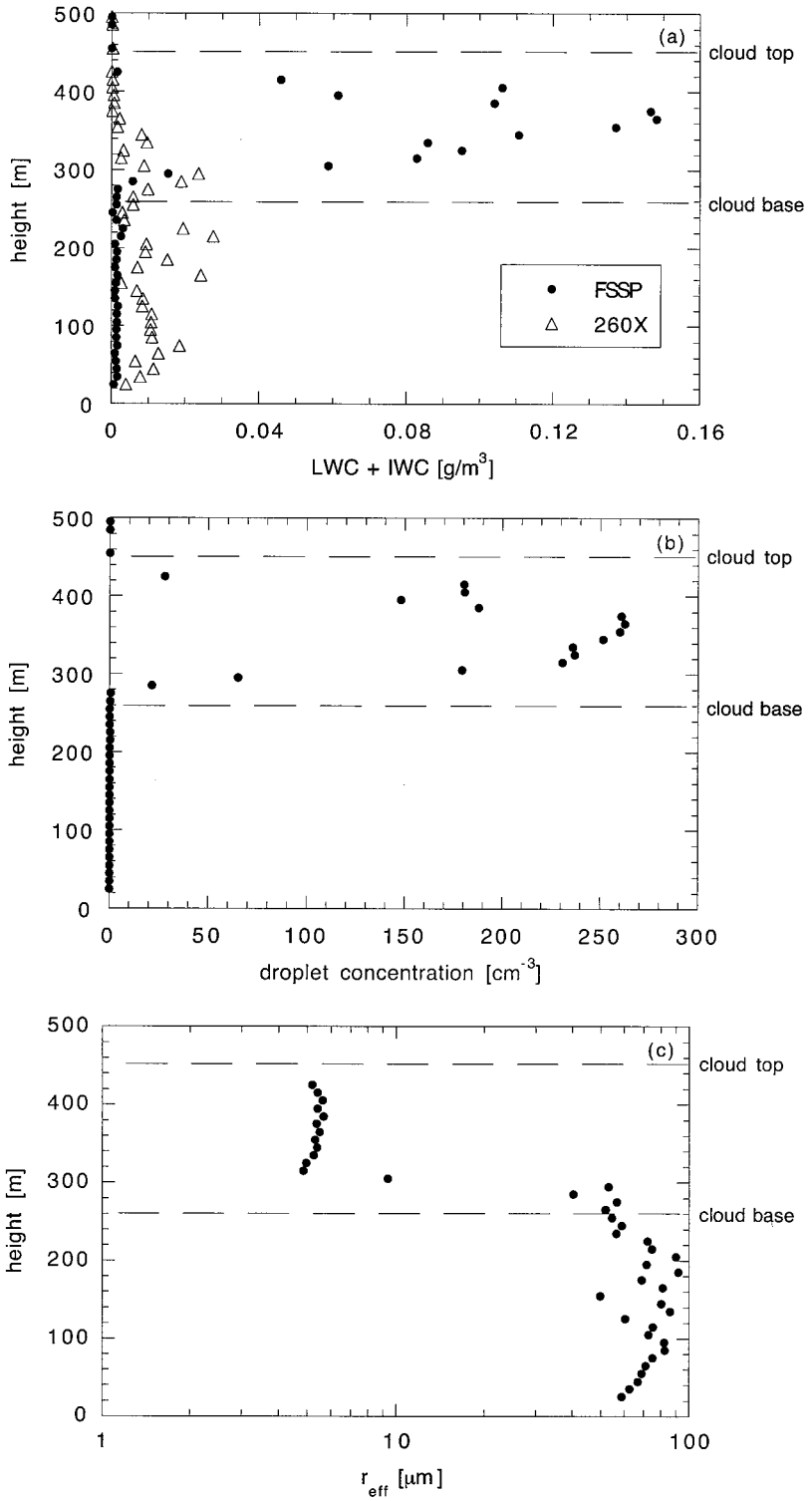

Figure 3. NCAR C-130 aircraft FSSP-100 and 260X data collected between 2106 and 0051 UTC just after a balloon sounding on May 7, 1998 (Figure 2). (a) Ice water content (IWC) and liquid water content (LWC). (b) Droplet concentration. (c) Cloud droplet effective radius. The balloon and aircraft measurements were made with a frequency of 0.1 Hz and 1 Hz, respectively. The aircraft speed was ~100 m s^{-1}.

slightly higher actinic flux above the cloud than do the observations, which probably can be explained by the fact that we neglected the effect of aerosols and ice crystals above the cloud layer.

5.2. Vertical Profiles

A summary of the tethered-balloon soundings made in arctic stratus between May 7 and 9, 1998, is presented in Table 1.

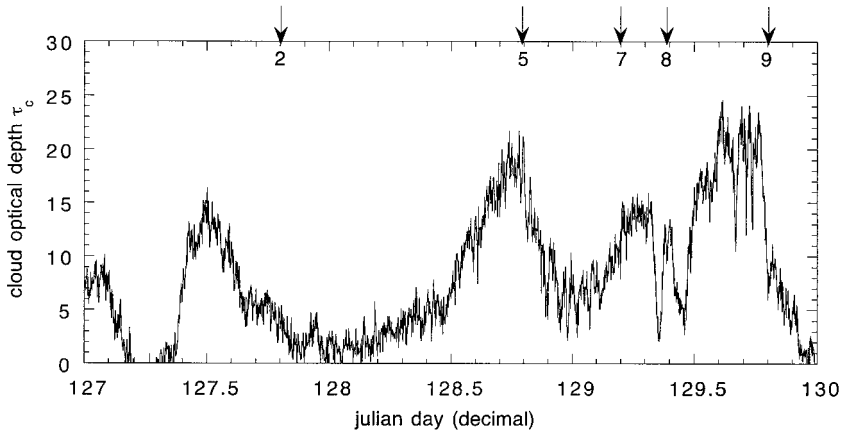

Figure 4. The total cloud optical depth τ_c as a function of time. The total cloud optical depth is computed from equation (14) where we used the liquid water path from the microwave radiometer and the effective radius according to the aircraft data. The times of the balloon soundings are indicated by arrows and numbered for easy referencing.

Table 1 also includes some characteristics of an Atlantic stratocumulus case. The actinic flux measurements made in this cloud, and discussed in detail by *Vilà-Guerau de Arellano et al*. [1994], will be compared with the observations made in arctic stratus.

To illustrate the effect of the solar zenith angles on the vertical profiles of the actinic fluxes, we show two examples of vertical actinic flux profiles in Figure 7. These were made above the arctic sea ice and from Santa Maria Island during the Atlantic Stratocumulus Transition Experiment (ASTEX). The ground albedo for UV-A during ASTEX was ~0.05. Although the two profiles were measured at a different wavelength (F_{365} and F_{550} for the Azores and arctic, respectively), the fraction of diffuse light due to Rayleigh scattering is about the same for both cases. According to a computation of the optical depth for Rayleigh scattering [*Slingo and Schrecker*, 1982], the fraction $\tau_{\mathrm{Ray}}/\mu_0$ gives 0.62 and 0.73 for the UV-A and visible radiation for the upward sounding, respectively. The measurements show that the UV-A actinic flux increases approximately linearly toward the cloud top. In contrast, the magnitude of the visible actinic flux changes rapidly in the upper 50 m of the cloud layer, while in the rest of the cloud the vertical variations are relatively small. Variations in μ_0 change the magnitude of the actinic flux but hardly affect the gross shape of the vertical profile.

The differences in the vertical profiles can be explained by means of a delta-Eddington model [*Meador and Weaver*, 1980]. Although more accurate models are available, in particular, for small μ_0, this simple model can help to qualitatively understand the observed vertical profiles of the actinic flux and can illustrate the theory presented in section 2. Four vertical profiles were computed, two of which were representative for the measurements shown in Figure 7, and two additional simulations were made in which we changed the ground albedo.

The effect of a larger ground albedo is to increase the actinic flux magnitude rather than to change the approximate shape of the vertical profile; the latter is more affected by the solar zenith angle (see Figure 8). For the two cases where $\mu_0 = 0.8$, the actinic flux increases from cloud base to a maximum just below the cloud top. This peak can be explained by an inspection of (13). The irradiance and actinic flux profiles as computed by the delta-Eddington model are exactly described by this formula. Between the level of the actinic flux maximum and cloud top we have $(d/d\tau)F_{\mathrm{tot}} > 0$, such that

$$E_0\left(\frac{1}{3\mu_0^2} - 1\right) > (1 - \omega_0 g)E_{\mathrm{tot}}. \tag{15}$$

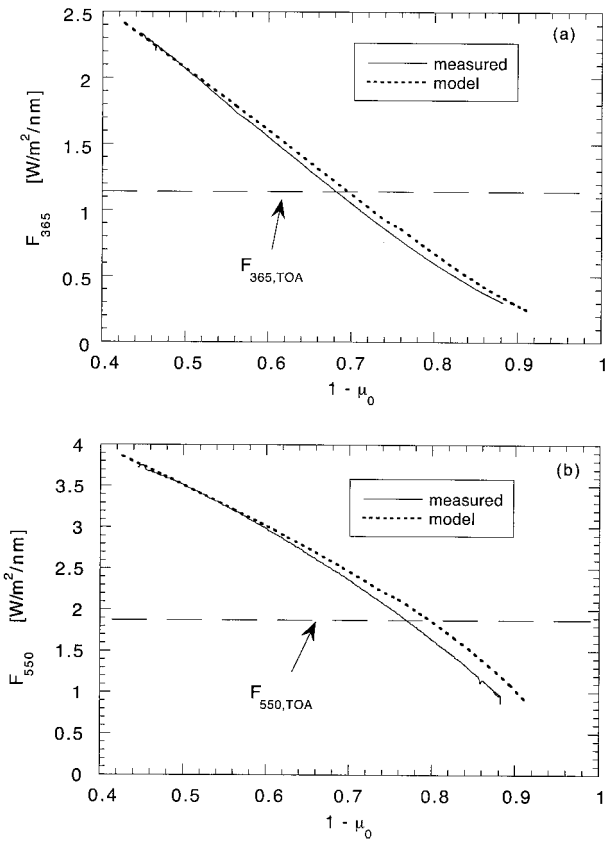

Figure 5. Diurnal cycle of modeled and measured actinic flux during clear skies as a function of $\mu_0 = \cos\theta_0$. (a) UV-A. (b) Visible. The line styles are according to the legend.

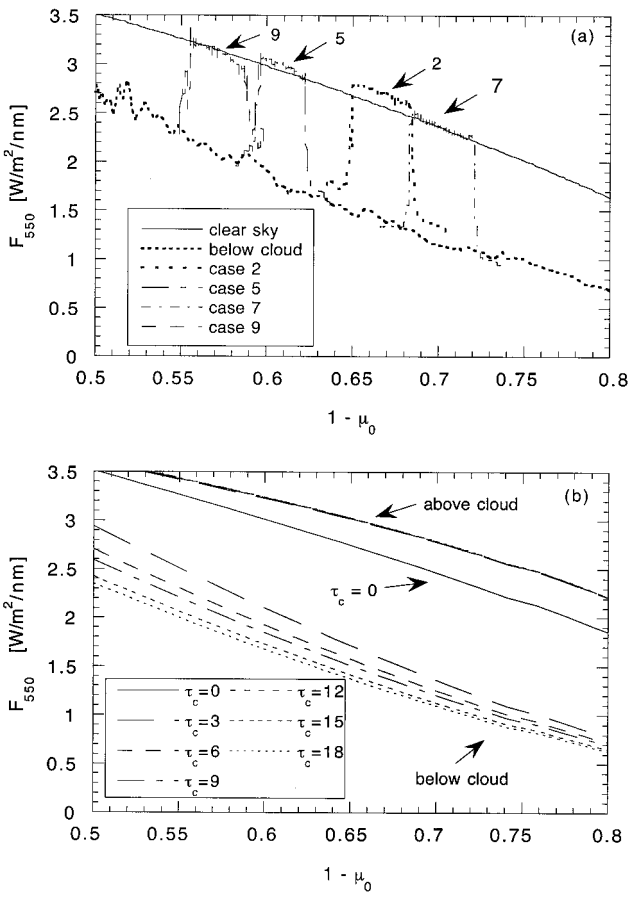

Figure 6. (a) Visible actinic flux from measurements made just above the surface and from four tethered-balloon soundings in arctic stratus. During the surface measurements, arctic stratus was present from Julian day 128.46 to 128.96. The balloon soundings are summarized in Table 1. (b) Model simulation of the visible actinic flux below and above the cloud for different values of the total cloud optical thickness (τ_c).

At the level of the actinic flux maximum these two terms balance. However, when the direct solar beam propagates into the cloud layer, E_0 gradually decreases according to (5). Below the actinic flux maximum, (15) no longer holds and the actinic flux decreases toward cloud base. For the arctic stratus cases the direct component of the solar beam E_0 enhances the downward decrease of the actinic flux in a shallow layer near the top of the cloud. Since μ_0 is so small for these cases, E_0 rapidly becomes negligibly small, and the vertical gradient of the actinic flux in the bulk of the cloud layer is determined primarily by the first term on the right-hand side of (13):

$$dF_{\text{tot}}/dt \approx 3(1 - \omega_0 g) E_{\text{tot}}. \quad (16)$$

The very small vertical gradient of the actinic flux in the lower part of the arctic cloud layer can be explained by two mechanisms. First, a rather low value of the total net irradiance is due to the low values of μ_0 in the arctic region. Second, the high surface albedo tends to reflect a large fraction of the incident downward radiation, causing the net irradiance to decrease according to (4).

Although the model results indicate a peak in the actinic flux for large μ_0 no clear peak value can be distinguished from the balloon sounding made from the Azores. This could be due to the fact that in a real cloud field the cloud tops are located at different heights such that the peak value is smoothed, whereas in the model a perfectly homogeneous cloud is assumed. Nevertheless, the basic features of the observed vertical profiles, such as the strong increase below the cloud top for small μ_0, can be explained qualitatively well by the delta-Eddington model.

6. Summary

The actinic flux is the radiative quantity that determines photodissociation rates in the atmosphere. During May 1998, actinic flux measurements were made above the arctic sea ice at the SHEBA camp by means of 4π radiometers. A visible (λ = 550 nm) 4π radiometer and a UV-A (λ = 365 nm) 4π radiometer were installed just above the surface, and they collected measurements continuously. During the period of observation the arctic sea ice region was characterized by the frequent occurrence of low stratus clouds. To collect measurements in these clouds, another visible 4π radiometer was attached to a tethered balloon. The balloon was launched at least once a day. A detailed assessment of the thermodynamic and microphysical structure of the stratus clouds could be made from an analysis of measurements made by the NCAR C-130 aircraft which made several flights in the vicinity of the SHEBA ice camp during the actinic flux measurement campaign. In addition, a microwave radiometer and a lidar were employed to provide data concerning the cloud liquid water path and cloud phase.

To investigate the diurnal cycle of the actinic flux during

Table 1. Cloud Characteristics for the Five Selected Tethered-Balloon Soundings Made Above the Arctic Sea Ice and Case 5 From *Vilà-Guerau de Arellano et al.* [1994] Measured During the ASTEX Experiment on Santa Maria Island on June 13, 1992, Azores (36.99°N, 25.17°W)[a]

Case	Start Julian Day (Decimal)	μ_0 Start	μ_0 End	τ_c	Cloud Type
2	127.73	0.30	0.36	5 ± 2	stratus
5	128.77	0.36	0.42	17 ± 4	stratus
7	129.17	0.33	0.27	12 ± 4	stratus
8	129.31	0.15	0.10	10 ± 4	stratus, thinning throughout experiment
9	129.80	0.40	0.45	8 ± 4	fog
Azores	165.66	0.85	0.74	23 ± 4	stratocumulus

[a]Values of μ_0 represent the cosine of the solar zenith angle at the start of the upward sounding and the end of the downward sounding. The cloud cover (N) for the arctic stratus cases was approximately unity, whereas the Atlantic stratocumulus case was mainly broken to overcast (N = 7 oktas and N = 8 oktas).

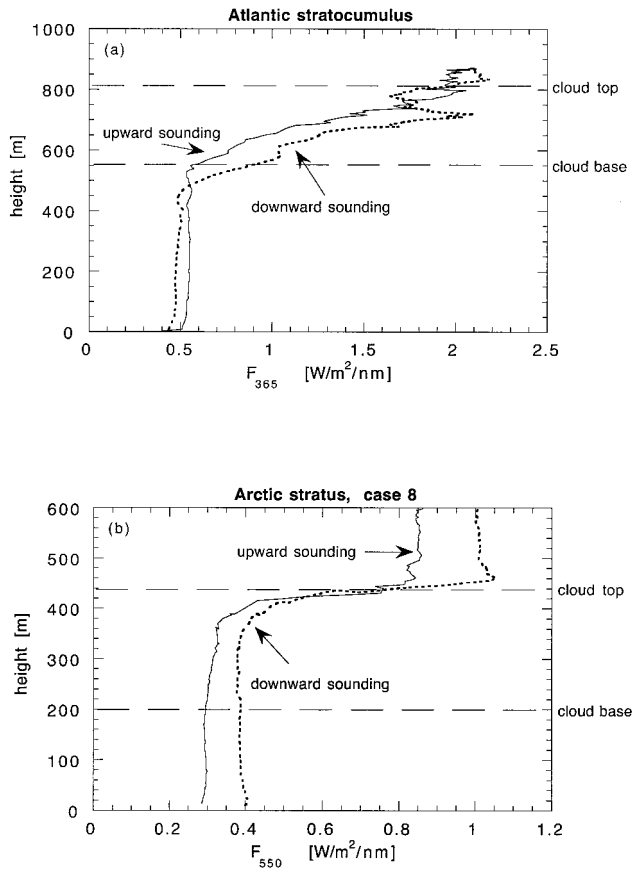

Figure 7. Measured vertical profiles of the actinic flux. (a) UV-A actinic flux in stratocumulus during ASTEX. (b) Visible actinic flux in arctic stratus above arctic sea ice (case 8 according to Table 1). The cloud base and cloud top height are also indicated. During the ASTEX stratocumulus sounding, the cloud base height descended when the balloon was descending, and the indicated cloud top and cloud base height were taken for the upward sounding.

clear-sky conditions, we made a data selection on the basis of visual observations and careful analysis of radar, microwave radiometer, and lidar data. The actinic flux was found to become smaller for decreasing μ_0. To verify whether the observed diurnal cycle could be explained by only Rayleigh scattering, we used a monochromatic radiative transfer model to simulate an atmosphere without clouds and aerosols. The model results agreed well with the observations, although the observed visible and UV-A actinic fluxes were found to be slightly smaller than the simulation results for smaller μ_0. It was suggested that this might be attributed to the effect of some aerosols and ice crystals with a small optical depth ($\tau \sim 0.1$). A comparison of the actinic flux measured above stratus clouds with the surface observations during the clear-sky conditions showed that they were almost the same. This could be attributed to the fact that the optical properties of the snow-covered ice surface resemble those of a cloud surface above a snow-covered ice surface.

Between May 7 and 9, 1998, a persistent arctic stratus layer was present above the SHEBA ice camp, and various balloon launches were made during this period. The NCAR C-130 collected measurements during this period as well. The temperature of the cloud layer was found to be rather low (about −18°C), and the cloud top was capped by a stable temperature inversion. Although the temperature in the cloud was well below 0°C, the values for the liquid water path of the cloud suggested that a significant quantity of the cloud droplets was supercooled. This finding was corroborated by the rather low depolarization ratios obtained by a lidar during this period, which are indicative of spherical liquid water droplets. The cloud droplet concentration was rather high (~250 cm^{-3}). This type of arctic stratus cloud layer was frequently observed during other aircraft flights made during the SHEBA project. *Curry et al.* [2000] suggested that the presence of ice particles in arctic clouds would be more likely if the cloud droplet concentration were rather low. Conversely, the cloud phase would tend to be liquid if there were a higher cloud droplet concentration (>100 cm^{-3}).

The vertical actinic flux gradient was found to be very small within the arctic stratus cloud, except in a shallow layer near the cloud top where the actinic flux significantly increased with height. If we assumed a plane-parallel cloud, a manipulation of the radiative transfer equation for the diffuse radiance could well explain the observed vertical in-cloud profile of the actinic flux. We argued that if the direct component of the radiation is negligibly small and if there is no absorption in the cloud, the actinic flux will decrease linearly from cloud top to the cloud base as a function of the optical depth. The slope of the vertical gradient is proportional to the magnitude of the net irradiance. Because the arctic stratus observations were made when μ_0 was rather small, the vertical actinic flux gradient was very small too. In addition, the absolute value of the irradiance is decreased by reflection of downwelling radiation at the snow-covered ice surface. In contrast, for large μ_0 and a much larger net irradiance, the actinic flux will significantly increase from the cloud base toward the cloud top, as was found by *Vilà-Guerau de Arellano et al.* [1994] for Atlantic stratocumulus. Deviations from this linear vertical actinic flux profile can be expected if the direct contribution of the direct solar radiation cannot be neglected. This is usually the case near the cloud top, where a rapid downward decrease in the direct component of the solar radiation causes a sharp jump in the actinic flux if $\mu_0^2 < 1/3$, as was observed in the arctic stratus clouds.

It has been demonstrated that a tethered balloon is a good platform to measure actinic fluxes. Since the actinic flux is intimately related to the irradiance, it is a valuable parameter

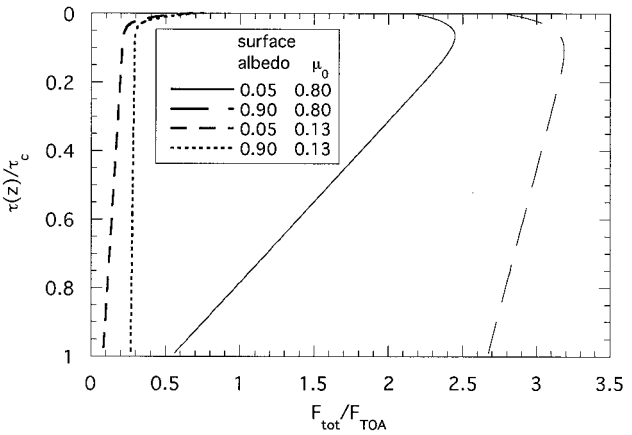

Figure 8. Vertical profiles of the actinic flux in the cloud layer, normalized with the incident actinic flux at the top of the atmosphere, calculated with the delta-Eddington model.

to measure during intensive field campaigns. For the observations discussed in this paper, radiative absorption was negligibly small. We have explained, however, that there is a simple relation between the magnitude of the actinic flux and the gradient of the irradiance. When the single scattering albedo is less than unity, actinic flux observations can be used to measure absorption profiles of the total net irradiance indirectly.

Acknowledgments. Michiel van Weele is thanked for assisting with the radiative transfer model. The first author was supported by the Netherlands Geosciences Foundation (GOA) with financial aid (grant 750.295.03A) from the Netherlands Organization for Scientific Research. The aircraft data collected by means of the C-130 of NCAR were kindly supplied by Ron Ruth and Krista Laursen. The authors thank NCAR and its sponsor, the National Science Foundation, for allowing them to use the observational data. The microwave radiometer data were kindly provided by J. Liljegren (Iowa State University). The satellite figures presented in this paper were made by D. Wylie (University of Wisconsin). Finally, the authors wish to thank the many people of the FIRE/SHEBA community for giving logistical support by bringing the equipment to the SHEBA ice camp and for assisting on the site.

References

Adler, R. F., R. A. Mack, N. Prasad, I. M. Hakkarinen, and H.-Y. M. Yeh, Aircraft microwave observations and simulations of deep convection from 18 to 183 GHz, part I, Observations, *J. Atmos. Oceanic Technol*., *7*, 377–391, 1990.

Crutzen, P. J., and P. H. Zimmermann, The changing photochemistry of the atmosphere, *Tellus*, *Ser. A and Ser. B*, *43*, 136–151, 1991.

Curry, J. A., et al., FIRE arctic clouds experiment, *Bull. Am. Meteorol. Soc*., *81*, 5–30, 2000.

Duynkerke, P. G., and S. R. de Roode, Surface energy balance and turbulence characteristics observed at the SHEBA ice camp during FIRE III, *J. Geophys. Res*., *106*, 15,313–15,322, 2001.

Duynkerke, P. G., H. Q. Zhang, and P. J. Jonker, Microphysical and turbulent structure of nocturnal stratocumulus as observed during ASTEX, *J. Atmos. Sci*., *52*, 2763–2777, 1995.

Goody, R. M., and Y. L. Yung, *Atmospheric Radiation: Theoretical Basis*, 2nd ed., 519 pp., Oxford Univ. Press, New York, 1989.

Grenfell, T. C., S. G. Warren, and P. C. Mullen, Reflection of solar radiation by the Antarctic snow surface at ultraviolet, visible, and near-infrared wavelengths, *J. Geophys. Res*., *99*, 18,669–18,684, 1994.

Herman, G. F., and J. A. Curry, Observational and theoretical studies of solar radiation in Arctic stratus clouds, *J. Clim. Appl. Meteorol*., *23*, 5–24, 1984.

Hobbs, P. V., and A. L. Rangno, Microstructures of low- and middle-level clouds over the Beaufort Sea, *Q. J. R. Meteorol. Soc*., *124*, 2035–2071, 1998.

Junkermann, W., Measurements of the $J(O^1D)$ actinic flux within and above stratiform clouds and above snow surfaces, *Geophys. Res. Lett*., *21*, 793–796, 1994.

Landgraf, J., and P. J. Crutzen, An efficient method for online calculations of photolysis and heating rates, *J. Atmos. Sci*., *55*, 863–878, 1998.

Liljegren, J. C., Two-channel microwave radiometer for observations of total column precipitable water vapor and cloud liquid water path, paper presented at Fifth Symposium on Global Change Studies, Am. Meteorol. Soc., Nashville, Tenn., 1994.

Los, A., M. van Weele, and P. G. Duynkerke, Actinic fluxes in broken cloud fields, *J. Geophys. Res*., *102*, 4257–4266, 1997.

Madronich, S., Photodissociation rates in the atmosphere, 1, Actinic flux and the effects of ground reflections and clouds, *J. Geophys. Res*., *92*, 9740–9752, 1987.

Madronich, S., UV radiation in the natural and perturbed atmosphere, in *Environmental Effects of UV (Ultraviolet) Radiation*, pp. 17–69, CRC Press, Boca Raton, Fla., 1993.

McKenzie, R. L., K. J. Paulin, and S. Madronich, Effects of snow cover on UV irradiance and surface albedo: A case study, *J. Geophys. Res*., *103*, 28,785–28,792, 1998.

Meador, W. E., and W. R. Weaver, Two-stream approximations to radiative transfer in planetary atmospheres: A unified description of existing methods and a new improvement, *J. Atmos. Sci*., *37*, 630–643, 1980.

Pinto, J. O., J. A. Curry, and K. L. McInnes, Atmospheric convective plumes emanating from leads, 1, Thermodynamic structure, *J. Geophys. Res*., *100*, 4621–4631, 1995.

Ruggaber, A., R. Forkel, and R. Dlugi, Spectral actinic flux and its ratio to spectral irradiance by radiation transfer calculations, *J. Geophys. Res*., *98*, 1151–1162, 1993.

Sassen, K., The polarization lidar technique for cloud research: A review and current assessment, *Bull. Am. Meteorol. Soc*., *72*, 1848–1866, 1991.

Shetter, R. E., C. A. Cantrell, K. O. Lantz, S. J. Flocke, J. J. Orlando, G. S. Tyndall, T. M. Gilpin, C. A. Fischer, S. Madronich, and J. G. Calvert, Actinometric and radiometric measurement and modeling of the photolysis rate coefficient of ozone to $O(^1D)$ during Mauna Loa Observatory Photochemistry Experiment 2, *J. Geophys. Res*., *101*, 14,631–14,641, 1996.

Slingo, A., and H. M. Schrecker, On the short-wave radiative properties of stratiform water clouds, *Q. J. R. Meteorol. Soc*., *108*, 407–426, 1982.

Stephens, G. L., The parameterization of radiation for numerical weather prediction and climate models, *Mon. Weather Rev*., *112*, 826–867, 1984.

Van der Hage, J. C. H., W. Boot, H. van Dop, P. G. Duynkerke, and J. Vilà-Guerau de Arellano, A photo-electric detector suspended under a balloon for actinic-flux measurements, *J. Atmos. Oceanic Technol*., *11*, 674–679, 1994.

Van der Hage, J. C. H., and S. R. de Roode, An isotropic light sensor for measurements of visible actinic flux in clouds, *J. Atmos. Oceanic Technol*., *16*, 1698–1701, 1999.

Van Weele, M., and P. G. Duynkerke, Effect of clouds on the photodissociation of NO_2: Observations and modelling, *J. Atmos. Chem*., *16*, 231–255, 1993.

Van Weele, M., J. Vilà-Guerau de Arellano, and F. Kuik, Combined measurements of UV-A actinic flux, UV-A irradiance, and global radiation in relation to photodissociation rates, *Tellus*, *Ser. B*, *47*, 353–364, 1995.

Vilà-Guerau de Arellano, J., P. G. Duynkerke, and M. van Weele, Tethered-balloon measurements of actinic flux in a cloud-capped marine boundary layer, *J. Geophys. Res*., *99*, 3699–3705, 1994.

Wiscombe, W. J., and S. G. Warren, A model for the spectral albedo of snow, 1, Pure snow, *J. Atmos. Sci*., *37*, 2712–2733, 1980.

Zeng, J., S. Madronich, and K. Stamnes, A note on the use of the two-stream delta-scaling approximation for calculating atmospheric photolysis rate coefficients, *J. Geophys. Res*., *101*, 14,525–14,530, 1996.

W. Boot, S. R. de Roode, P. G. Duynkerke, and J. C. H. van der Hage, Institute for Marine and Atmospheric Research Utrecht, Utrecht University, Princetonplein 5, 3584 CC Utrecht, Netherlands. (roode@phys.uu.nl)

(Received July 24, 2000; revised March 9, 2001;
accepted March 23, 2001.)